Detection of non-aqueous phase liquid contamination by SH-TE seismoelectrics: A computational feasibility study

Federico D. Munch [a,c], Fabio I. Zyserman [a,b,]*

[a] Facultad de Ciencias Astronómicas y Geofsicas, Universidad Nacional de La Plata, Paseo del Bosque s/n, 1900 La Plata, Argentina
[b] CONICET, Argentina
[c] CICPBA, Argentina

ARTICLE INFO

ABSTRACT

In this work we propose a one dimensional numerical study of the seismoelectric signals produced in a fresh water aquifer contaminated by either light or dense non-aqueous phase liquids ((L/D)NAPLs), considering a pure SH-wave seismic source. We investigate the nature of the electromagnetic response generated at media interfaces, the so called Interface Response (IR), by comparing it with the electromagnetic field generated by a current sheet; wherefrom we are able to interpret that the source of the IR behaves as an electric current flowing along the interface, differently to what happens when the IR is originated by the action of a P-wave, where electric charge accumulation generates an electric dipole. We perform a parametric study to analyze how the presence of contaminants affects the IR, resorting to an effective media approach to compute mechanical and electromagnetic properties, and considering three different effective fluid-saturation dependent electrokinetic coupling coefficient models. We observe, as expected, that porosity plays an important role in the amplitude of the IRs. When considering different NAPL saturations, significant effects on the IRs are only seen when the thickness of the contaminated layer is above a threshold value, which depends on the present contaminant and the considered effective electrokinetic coupling coefficient model.

© 2016 Elsevier B.V. All rights reserved.

1. Introduction

Non-aqueous phase liquids (NAPLs) are hydrocarbons that exist as a separate, immiscible phase when in contact with water and/or air. Differences in the physical and chemical properties of water and NAPL result in the formation of a physical interface between the liquids which prevents the two fluids from mixing (Newell et al., 1995). Non-aqueous phase liquids are typically classified by density. Dense NAPL (DNAPL) consists of a solution of organic compounds (e.g., chlorinated hydrocarbons) that are denser than water; therefore, DNAPLs would sink to the bottom of an aquifer. In contrast, a light NAPL (LNAPL) consists of a solution of organic compounds (e.g., petroleum hydrocarbons) which is less dense than water and forms a layer that floats on the surface of the groundwater table (Mayer and Hassamozadesh, 2005; Carcione et al., 2003). The most common NAPL-related groundwater contamination problems result from the release of petroleum products into the soil. Success or failure of a NAPL remediation program depends in large measure on the remediation objectives and adequacy of the site characterization (Newell et al., 1995). The focus of site characterization is often to determine the subsurface contamination distribution in the aquifer, NAPL properties and other pertinent fluid/media properties (Newell et al., 1995; Environmental Protection Agency, 1994). Several authors have investigated the effects of NAPLs on mechanical and electromagnetic (EM) properties (Smeulders et al., 2013; Carcione et al., 2003) concluding that the acoustic and electromagnetic properties of soils saturated with air, water and hydrocarbons show significant variations, depending on the degree of saturation of the different fluids.

Noninvasive methods can often be used during the early phases of field work to optimize the cost-effectiveness of a NAPL site characterization program (Environmental Protection Agency, 1994). Although ground-penetrating radar, EM conductivity and complex resistivity have been applied to site characterization (Benson et al., 1982; Davis, 1991; Walther et al., 1986), those studies were not focused on the direct detection of NAPLs.

Although the seismoelectric effect has been known for decades (Ivanov, 1939; Frenkel, 1944), it was after the work of Pride (1994), where a closed formulation for seismoelectrics was presented, that this area has achieved new interest. Further theoretical advances have been presented (Pride and Haartsen, 1996; Haartsen and Pride, 1997; Garambois and Dietrich, 2002; Revil et al., 2007), along with modeling developments (Hu et al., 2007; Zyserman et al., 2010; Gao and Hu, 2010; Schakel et al., 2011, 2012; Ren et al., 2012; Yamazaki, 2012;

* Corresponding author at: Facultad de Ciencias Astronómicas y Geofsicas, Universidad Nacional de La Plata, Paseo del Bosque s/n, 1900 La Plata, Argentina.
  E-mail address: zyserman@fcaglp.unlp.edu.ar (F.I. Zyserman).

Zyserman et al., 2012; Warden et al., 2013; Guan et al., 2013), a series of successful field experiments (Butler, 1996; Garambois and Dietrich, 2001; Thompson et al., 2005, 2007; Dupuis et al., 2007; Haines et al., 2007a; Dupuis et al., 2009) and laboratory experiments (Bordes et al., 2006, 2008; Allègre et al., 2010, 2015), where we are mentioning just a few works in each area. According to the theory, the seismoelectric method could combine a high spatial resolution, comparable to that of seismics, with the sensitivity of electrical methods to hydrological properties of the subsurface (Dupuis and Butler, 2006; Haines et al., 2007a). As it is presently well known, seismoelectrical signals are electrokinetically generated by the propagation of seismic waves within a porous material in which an electrical double layer (EDL) can be developed. They can be recorded using a seismic source and electric receivers. Recent field studies have focused on the seismoelectric conversions linked to electrokinetics in order to investigate oil and gas reservoirs (Thompson et al., 2005) or hydraulic reservoirs (Dupuis et al., 2009; Haines et al., 2007a, 2007b; Strahser et al., 2011; Garambois and Dietrich, 2001). These investigations have shown that not only the depth of the reservoir can be deduced, but also the geometry of the reservoir can be imaged using the amplitudes of the electroseismic signals (Thompson et al., 2007). As pointed out in Jouniaux and Ishido (2012) and Jouniaux and Bordes (2012), this method is especially appealing to hydrogeophysics for the detection of subsurface interfaces induced by contrasts in permeability, porosity or electrical properties (salinity and water content).

Following this line, the aim of this work is to determine whether shear wave driven seismoelectrics can provide useful information to determine the presence of NAPLs, either dense or light, in fresh water aquifers. We start our work by reviewing the most important theoretical concepts of seismoelectrics, and follow by giving a full description of the effective medium approach employed to compute the mechanical and electromagnetic properties of the analyzed media. Next, we consider a pure SH seismic source and propose 1D models to simulate the presence of light or dense NAPLs. For these models, we use a one dimensional finite element formulation to approximate the solution to Pride's equations, and study the sensitivity of the Interface Responses to changes in relevant parameters such as porosity, NAPL saturation, thickness of the contaminated layer and viscosity.

2. Theoretical background

When a compressional wave travels through a porous medium, it creates a fluid-pressure gradient and an acceleration of the solid matrix, inducing a charge separation at the scale of the seismic wavelet, due to the presence of an EDL, that in turn yields an electrical potential difference. The generated electric field, which travels within the passing compressional seismic waves, is known as the coseismic wave. Another type of seismoelectric conversions arises when a seismic wave crosses a contrast between mechanical or electrical properties (Haartsen and Pride, 1997; Block and Harris, 2006; Chen and Mu, 2005). At such interface an electromagnetic wave – known as the Interface Response (IR) – emerges, potentially providing information about the contrasts in the medium properties at depth. Pride (1994) derived the equations governing the coupled seismic and electromagnetic wave propagation in fluid-filled porous media – fully detailed in Appendix B – by combining Maxwell's equations with Biot's equations for poroelasticity (Biot, 1956a, 1956b). Two coupled transport equations were derived (Eqs. 251 and 252 in Pride (1994))

$$\boldsymbol{J} = \sigma(\omega)\boldsymbol{E} + L(\omega)\left(-\nabla p + \omega^2 \rho_w \boldsymbol{u^s}\right) \tag{1}$$

$$-i\omega\boldsymbol{u^f} = L(\omega)\boldsymbol{E} + \frac{\kappa(\omega)}{\eta_w}\left(-\nabla p + \omega^2 \rho_w \boldsymbol{u^s}\right). \tag{2}$$

The macroscopic electrical current density $\boldsymbol{J}$ [A/m^2] is given in Eq. (1) as the sum of the average conduction and streaming current densities, respectively the first and second terms of its right-hand-side. In Eqs. (1)–(2) an $e^{-i\omega t}$ time dependence of the propagating wave is assumed, being ω [rad/s] the angular frequency. The vector function $\boldsymbol{E}$ [V/m] is the electric field and $\sigma(\omega)$ [S/m] denotes the frequency-dependent conductivity of the material. In both equations, p [Pa] is the pore-fluid pressure, ρ_w [kg/m^3] is the density of the fluid (water), and $\boldsymbol{u^s}$ [m] and $\boldsymbol{u^f}$ [m] denote the solid and the average relative fluid displacements. The dynamic viscosity of the fluid is written as η_w [Pa s] and $\kappa(\omega)$ [m^2] indicates the frequency-dependent permeability. We write the complex frequency-dependent coupling $L(\omega)$ linking Eqs. (1) and (2) as

$$L(\omega) = L_0 \mathcal{F}(\omega). \tag{3}$$

In Eq. (3), $F(\omega)$ introduces the frequency dependence and L_0 denotes the low frequency electrokinetic coupling, whose expression is given in Appendix A; its water saturation dependent version, as introduced by Warden et al. (2013), is given in Section 3.5. Please notice that when this coefficient is set to zero, the poroelastic wave equations are completely decoupled from the electromagnetic ones. It is also worthwhile to recall that Pride's theory requires the validity of the so called "thin double-layer approximation", meaning that the Debye length, which is a measure of the thickness of the diffuse double layer, is much smaller than any geometrical length associated with the porous material (Pride, 1994). This assumption is no longer valid, for example, in clayey soils (Block and Harris, 2006). Other authors proposed an alternative model, using either the excess of electrical charge in the pore space or a relationship between an effective excess of charge and permeability to model electrokinetic processes (Revil and Linde, 2006; Linde et al., 2007; Revil et al., 2007; Revil and Jardani, 2010; Jougnot and Linde, 2011). One of both approaches have been used, for example, by Revil et al. (2013) to show how a saturation front characterized by a drop in the electrical conductivity and compressibility is responsible for seismoelectric conversions, and by Jougnot et al. (2013) to characterize seismoelectric effects due to mesoscopic heterogeneities. However, Jackson and Leinov (2012) demonstrated that certain soil conditions lead also to the failure of the thick double layer approximation and recent experimental results show that under saturated conditions only at lower salinities rock permeability and pore radius can be well recognized from the amplitude of electrokinetic signals (Wang et al., 2015). The undergoing efforts may lead finally to a better seismoelectric theory in the future; but presently, Pride's theory is still among the best sets of accepted governing equations for seismoelectric coupling (Hu and Gao, 2011), so we choose it for our modeling, being careful in considering parameters so that its validity requirements are completely fulfilled.

Pride's equations, in their original form, cannot deal with partial saturation conditions. In order to enable the treatment of such situations, we use the approach provided by the effective medium theory, which replaces the multiphasic fluid occupying the pore space by a homogeneous fluid of equivalent effective properties (Gueguen and Palciauskas, 1994). We will further discuss the mixing laws used to estimate the medium effective mechanical properties as a function of water saturation in Section 3. It should be taken into account that the õeffective medium approach must be carefully applied to compute the medium properties. For example, the electrical conductivity of a water/NAPL mixture may not be determined as the weighted average of the conductivities of each individual phase due to the fact that, under partial saturation condition, the electrical current preferentially flows in the water phase; as a consequence, expressions for the saturation-dependent conductivity taking the formation factor into account are needed (Revil et al., 2007; Jackson, 2010). The laws used to compute the medium electrical properties in partial saturation conditions are detailed in Section 3.4.

3. Effective model parameters

3.1. Bulk density and viscosity

The effective bulk density ρ_b[kg/m3] of a porous rock composed of two minerals and two fluids is calculated by means of the arithmetic average

$$\rho_b = (1-\phi)\rho_s + \phi\rho_{ef}, \tag{4}$$

where:

$$\rho_s = \rho_{qz}\gamma_{qz} + \rho_{sh}\left(1-\gamma_{qz}\right) \quad \text{and} \quad \rho_{ef} = S_w\rho_w + (1-S_w)\rho_{NAPL}. \tag{5}$$

In these equations S_w denotes water saturation, ρ_s the average density of the solid grains, with ρ_{qz} and ρ_{sh} the quartz and shale densities respectively, γ_{qz} is the volume fraction of quartz and ϕ is the porosity. It is worth mentioning that, as we consider a mineral frame composed of two constituents, the condition $\gamma_{sh} + \gamma_{qz} = 1$ must be satisfied. Besides, ρ_{ef} is the average density of the poral fluids, with ρ_w and ρ_{NAPL} the mass densities of
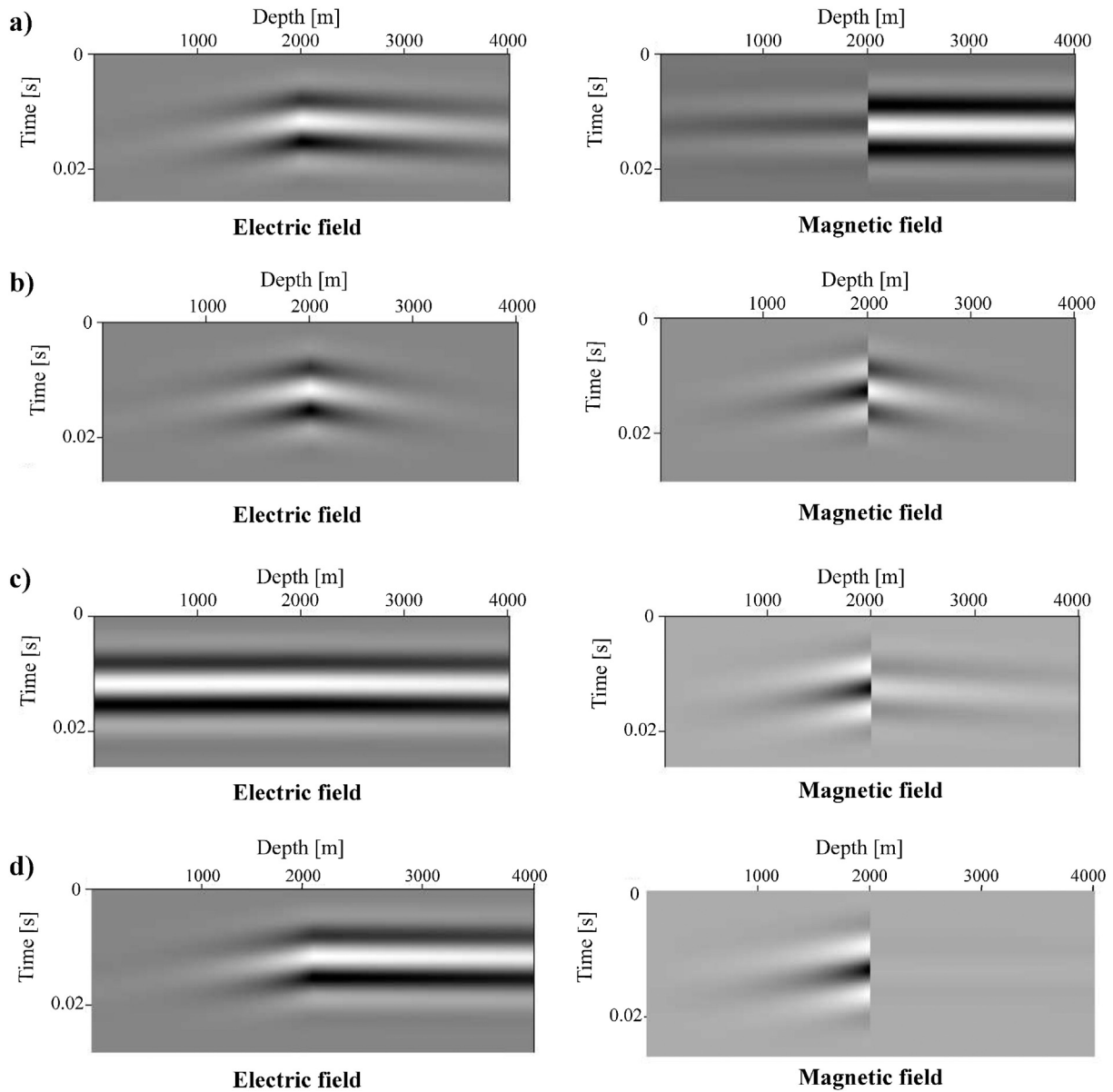

Fig. 1. Electric (left) and magnetic (right) responses obtained solving Maxwell's equations for an infinite current sheet directed along x located at a depth $z_f = 2000$ m and 401 dipole receivers – set 10 m apart – are deployed inside a vertical uncased borehole, as described in Section 4, considering: a) homogeneous medium with conductivity $\sigma = 10^{-7}$ [S/m]. b) a homogeneous medium with conductivity $\sigma = 10^{-2}$ [S/m]. c) one layer, 2000 m thick with conductivity $\sigma_1 = 10^{-2}$ [S/m], set on top of a half-space with conductivity $\sigma_2 = 10^{-3}$ [S/m]. d) the same geometry considered in c) except that in this case we consider $\sigma_1 = 10^{-2}$ [S/m] and $\sigma_2 = 10^{-5}$ [S/m].

water and NAPL, respectively. It is worth noting that we assume ambient pressure and temperature conditions, this assumption implies that anomalously high temperature and pressure gradients are second-order effects that we do not consider in this work. For greater depths, as it is mentioned in Warden et al. (2013), empirical laws expressing the mass densities as a function of temperature and pressure, such as those proposed by Blatze and Wang (1992) or Mavko et al. (2009), should be considered.

We use the expression derived by Teja and Rice (1981) to determine the effective viscosity η[Pa·s] of the water/NAPL mixture, which reads

$$\eta = \eta_{\text{NAPL}} \left(\frac{\eta_{\text{w}}}{\eta_{\text{NAPL}}} \right)^{S_{\text{w}}}. \tag{6}$$

Here η_{NAPL} and η_{w} are water and NAPL viscosities, respectively. In case of a water/air mixture, we replace η_{NAPL} with η_{air}. Fluid properties considered in this paper are detailed in Table 2. It is worth mentioning that we do not use this effective viscosity in the expression of the static seismoelectric coupling L_0, for which the viscosity of water is taken instead, as we assume water as the wetting phase.

3.2. Shear modulus

Following Mavko et al. (2009), the Voigt–Reuss–Hill average G_s[GPa] is used to estimate the effective elastic moduli of a rock in terms of its constituents

$$G_s = \frac{G_v + G_r}{2}. \tag{7}$$

Considering a rock composed of quartz and shale

$$G_v = \left(1 - \gamma_{\text{qz}}\right) G_{\text{sh}} + \gamma_{\text{qz}} G_{\text{qz}} \quad \text{and} \quad \frac{1}{G_r} = \frac{1 - \gamma_{\text{qz}}}{G_{\text{sh}}} + \frac{\gamma_{\text{qz}}}{G_{\text{qz}}}. \tag{8}$$

In the above expressions G_{sh} and G_{qz} are the shear modulus of shale and quartz, respectively. We assume that $G_{\text{sh}} = 20$ GPa and $G_{\text{qz}} = 39$ GPa (Schön, 1996).

In addition, following Pride (2005), the shear bulk modulus G_b can be estimated by the expression

$$G_b = G_s \frac{1 - \phi}{1 + 3c\phi/2}, \tag{9}$$

where the parameter c is called the "consolidation parameter", since it characterizes the degree of consolidation between the grains. Depending on the degree of cementation, one can expect the approximate range $2 < c < 20$, for consolidated sandstones (2 being extremely consolidated and 20 poorly consolidated). An unconsolidated sand in this model can require $c \gg 20$, in which case it may be more appropriate to use Walton's theory Pride (2005). In this paper, we assume that $c = 10$ in order to model a moderate degree of consolidation.

3.3. Dynamic permeability

Johnson et al. (1987) determined the nature of the flow in the high-frequency limit where viscous-boundary layers become so thin as to be considered locally planar relative to the curved grain surfaces. They connected this exact high-frequency limit to the low-frequency limit using a simple frequency function that respects causality constraints. Their final model, as expressed in (Pride, 2005), is

$$\kappa(\omega) = \kappa_0 \left[\sqrt{1 + i \frac{4\omega}{n_j \omega_j}} + i \frac{\omega}{\omega_j} \right]^{-1}, \tag{10}$$
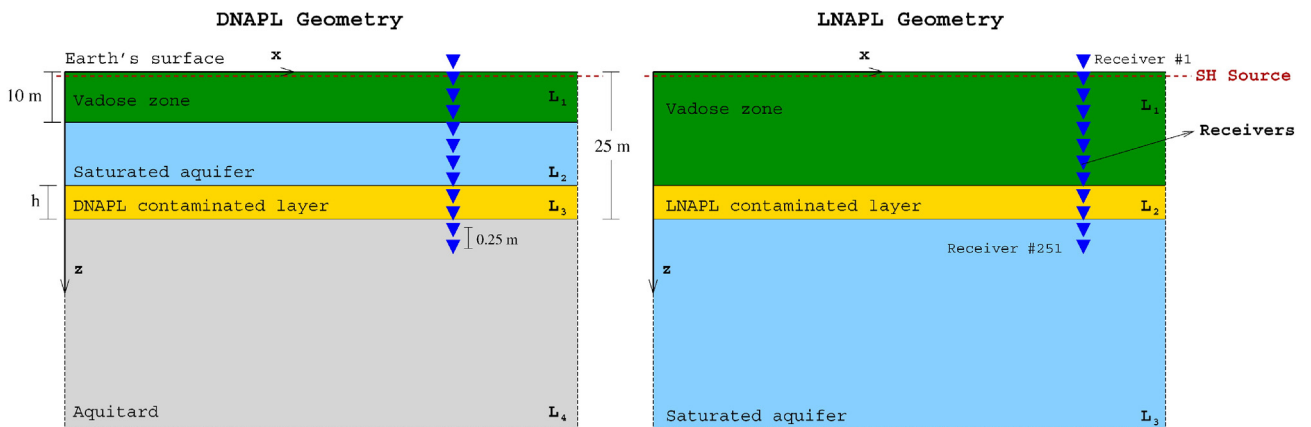

Fig. 2. Tabular models and seismoelectric vertical profiling layout considered to model the presence of DNAPL (left) or LNAPL (right). In both cases, the source is oriented along x and 251 dipole receivers – set 0.25 m apart – are deployed inside a vertical uncased borehole. Notice that L_i denotes the i-th layer, whose mineral frame and fluid content are detailed in Table 1.

where $i = \sqrt{-1}$ and n_j is an experimentally determined constant, which as in Zyserman et al. (2012), we take equal to 4 for the materials considered in this paper. The relaxation frequency ω_j, which controls the frequency at which viscous-boundary layers first develop, is given by

$$\omega_j = \frac{\eta}{\rho_{ef} F \kappa_0}. \tag{11}$$

Here, $F = \phi^{-m}$ is the formation factor, κ_0 corresponds to the value of dynamic permeability at low frequency limit and ρ_{ef} is the effective fluid density. We estimate κ_0 by using the Kozeny–Carman relation

$$\kappa_0 = B \frac{\phi^3}{(1-\phi)^2} d_k^2 \quad \text{where} \quad \frac{1}{d_k} = \frac{1}{r_{sh}} + \frac{1}{r_{qz}}. \tag{12}$$

Here B is a geometric constant (we assume that $B = 0.003$ (Carcione and Picotti, 2006)), r_{sh} and r_{qz} are the radii of the shale and quartz particles, respectively (Mavko et al., 2009).

Extensive tests (Rumpf and Gupte, 1971; Dullien, 1991) on laboratory data for granular media with mixed particle sizes (poor sorting) suggest that the Kozeny–Carman relation can still be applied using an effective or average particle size $\overline{D}$, defined by

$$\frac{1}{\overline{D}} = \frac{\gamma_{qz}}{D_{qz}} + \frac{\gamma_{sh}}{D_{sh}} \quad \text{with} \quad D_i^3 = \frac{7}{6} r_i^3, \tag{13}$$

where r_i is the radius particle of the i-th constituent; being $r_{qz} = 240 \, \mu m$ and $r_{sh} = 80 \, \mu m$ (Mavko et al., 2009).

3.4. Electrical conductivity

Assuming that NAPLs are insulators, it is possible to express the electrical conductivity [S/m] for partial saturated media as (Warden et al., 2013)

$$\sigma(S_w, \omega) = \frac{S_w^n}{F} \sigma_w + \frac{2}{F} \frac{C_{em} + C_{os}(\omega)}{\Lambda}, \tag{14}$$

where n is Archie's saturation exponent and σ_w denotes water conductivity. The cementation exponent m, related to the poral topography, is considered $m = n = 2.05$, according to its ranges given in Lesmes and Friedman (2005). The second fundamental porous-material geometry term Λ can be obtained from the expression (Pride, 1994)

$$\frac{\tilde{\xi} \alpha_\infty \kappa(\omega)}{\phi \Lambda^2} = 1. \tag{15}$$

Here $\alpha_\infty = \phi F$ denotes the tortuosity and the constant $\tilde{\xi}$, which takes values between 8 and 12 depending on poral geometry, is considered equal to 8.

The first term in Eq. (14) is the bulk conductivity while the second term denotes the surface conductivity. The latter is the combination of two different effects: C_{em} represents the excess conductance associated with the electromigration of double layer ions, while $C_{os}(\omega)$ is the frequency-dependent electroosmotic conductance due to the electrically induced streaming of the excess double-layer ions (their expressions can be found in Appendix A). In this way, Pride's frequency-dependent formula is combined with Archie's law, developed under static conditions, yielding the conductivity as a function of both water saturation and frequency (Warden et al., 2013). We consider here that the surface conductivity is independent of water saturation S_w (Brovelli et al., 2005). Besides, the contributions of C_{em} and C_{os} are not significant for clean sands, for which the volume-to-surface ratio is too large. These terms, whose expressions can be found in Appendix A, are important for clays since their specific surface area is orders of magnitude greater than the specific surface area of clean sands (Carcione et al., 2003).

Following Lesmes and Friedman (2005), σ_w is given by

$$\sigma_w = \sum_{l=1}^{2} (e z_l)^2 b_l N_l, \tag{16}$$

where e [C] is the electric charge of the ions, z_l is the valence, b_l [m/s] is the mobility [Nsm^{-1}] and N_l [l^{-1}] is the bulk ionic concentration. We estimate the mobility by an expression based on Stoke's law describing the motion of a sphere in a viscous medium (Warden et al., 2013; Pride and Morgan, 1991)

$$b_l = \frac{z_l}{6\pi \eta_w R_l}, \tag{17}$$

here l refers to the considered species, while R_l is its ionic radius [m]. Considering that charge transport in salt water is due to conduction of Na$^+$ and Cl$^-$, in our analysis, $R_{Na^+} = 1.83 \cdot 10^{-10}$ m for sodium and $R_{Cl^-} = 1.20 \cdot 10^{-10}$ m for chloride (Pride and Morgan, 1991); more details can be found in Appendix A.

3.5. Electrokinetic coupling

Several studies (Carcione et al., 2003; Smeulders et al., 2013) indicate that the presence of NAPL affects the effective electromagnetic properties, in particular, it affects the electrokinetic coupling. However, closed models to describe that behavior have not been yet developed. Therefore, in order to

introduce the effects of NAPLs on L_0, we adopt from Warden et al. (2013) the following expression for this important parameter

$$L_0(S_w) = -\frac{\epsilon_w \zeta}{\eta_w F}\left(1-2\frac{d}{\Lambda}\right)S_w^n C(S_w).$$

(18)

Here, η_w is the viscosity of water, ζ [V] is the zeta potential and the quantity d [m] denotes the Debye length, whose expression is detailed in Appendix A. In this equation $C(S_w)$ is a function relating the streaming potential coefficient obtained under partial saturation conditions to the one corresponding to full saturation conditions; we recall that we are assuming water as the wetting phase. Several authors have investigated this relation: Linde (2009) and Jackson (2010) proposed theoretical models suggesting that the coupling coefficient could be either monotonic or non-monotonic depending on the properties of the saturating phases; Perrier and Morat (2000) conducted field measurements and Guichet et al. (2003); Revil et al. (2007) and Strahser (2007) performed laboratory experiments which led them to predict – different – but monotonic behaviors with saturation. Allègre et al. (2010) and Allègre et al. (2012) while studying laboratory drainage experiments observed and modeled a non-monotonic behavior for the concerned coefficient. We select for the present work three expressions for $C(S_w)$ displaying a qualitatively distinct behavior, meaning monotonic and non-monotonic

$$C(S_w) = \begin{cases} \dfrac{1}{S_w^n} & \text{C-Model} \\[2ex] \dfrac{1}{S_w^n}\left(\dfrac{S_w-S_{wr}}{1-S_{wr}}\right)^2 & S_{wr}=0.10 \quad \text{PM-Model (Perrier and Morat, 2000)} \\[2ex] \left(\dfrac{S_w-S_{wr}}{1-S_{wr}}\right)\left[1+32\left(1-\left(\dfrac{S_w-S_{wr}}{1-S_{wr}}\right)\right)^{0.4}\right] & S_{wr}=0.10 \quad \text{Al-Model (Allègre et al., 2010)} \end{cases}$$

The $\mathcal{C}$-Model implies that there is no change in the electrokinetic coupling coefficient due to the presence of the contaminant. Although this model, in principle, contradicts experimental results, it is chosen in order to analyze the effectiveness of the technique even if there is no change in L_0 due to the NAPL. The PM-Model is valid strictly for non-polar contaminants, which cannot support an excess of charge associated with electrical double layers. This may not represent real oil-wetting conditions, however, as established by Jackson (2010), it is a reasonable first approach. In the case of Al-Model, this assumption may not be necessary because Allègre et al. (2015) associate the non-monotic behavior with the generation of an electrical double layer at the air/water interface. Alternative models to the latter have been proposed by other authors, while studying partial saturation conditions, both in laboratory and on field experiments, see for example Jougnot et al. (2012); Jougnot and Linde (2013); and Jougnot et al. (2015).

Following Zyserman et al. (2010), in Eq. (18) we use the permittivity of the wetting phase ($\epsilon_w = 80\ \epsilon_0$). According to Pride (1994), variations in the magnetic susceptibilities are assumed negligible in both the fluid and solid phases (iron, nickel and cobalt are not assumed to be major constituents), so we simply set $\mu = \mu_0$. As we are assuming water as the wetting phase, the ζ potential can be considered to be the zeta potential of a porous medium fully saturated with water (Zyserman et al., 2010; Warden et al., 2013). Following Pride and Morgan (1991), ζ potential can be expressed as a function of salinity (c_w [mol/l]) as

$$\zeta = 0.008 + 0.026 \ \log_{10}(c_w).$$

(19)

Salt concentration can also be expressed in ppt (parts per thousand). The relation is ppt $= 58.443\ c_w/\rho_w$, where 58.443 is the molecular mass of NaCl in g and ρ_w is given in g/cm³. Recall that for fresh waters, the concentration is <1 ppt, and for brines, the concentration is >35 ppt, being the average value in seawater 35 ppt (Carcione et al., 2003). Here we assume that $c_w = 1$ ppt in order to simulate a fresh water aquifer.

4. Pure EM case: infinite current sheet source

As it is known, the Interface Response is generated when a seismic wave crosses a contrast between mechanical or electrical properties (Haartsen and Pride, 1997; Block and Harris, 2006; Chen and Mu, 2005). In this situation, for a compressional wave, a transient localized charge separation across the interface is created. This secondary source can be approximated as an electrical dipole oscillating at the center of the first Fresnel zone (Thompson and Gist, 1993; Garambois and Dietrich, 2002). Haines and Pride (2006) stated that a shear wave will produce an imbalance of electrokinetic current across the interface that will lead to charge accumulation on one side of the interface and depletion on the other; thus, like a compressional wave, will induce electric dipoles at an interface. According to this point of view, for the one dimensional geometry considered in this paper, two charged planes of opposite sign would be expected at the interface; consequently, as the electric field generated by an infinite capacitor, the IR would be different from zero only between the charges, i.e., across and near the interface. However, as it can be seen below in the Results section, the obtained IRs do not display this behavior. In order to propose a

Table 1
Properties of the models proposed in Section 5.

	γ_{qz}	ϕ	Thickness [m]	S_w
DNAPL scenario				
L_1	0.85	0.2;0.27;0.35	10	0.20
L_2	0.85	0.2;0.27;0.35	$15-h$	1
L_3	0.85	0.2;0.27;0.35	$h = 0.1$ to 0.7, step: 0.1	0.1 to 1, step: 0.1
L_4	0.60	0.07	∞	1
LNAPL scenario				
L_1	0.85	0.2;0.27;0.35	$25-h$	0.20
L_2	0.85	0.2;0.27;0.35	$h = 0.1$ to 0.7, step: 0.1	0.1 to 1, step: 0.1
L_3	0.85	0.2;0.27;0.35	∞	1

Table 2
Physical properties of the fluids considered in this work.

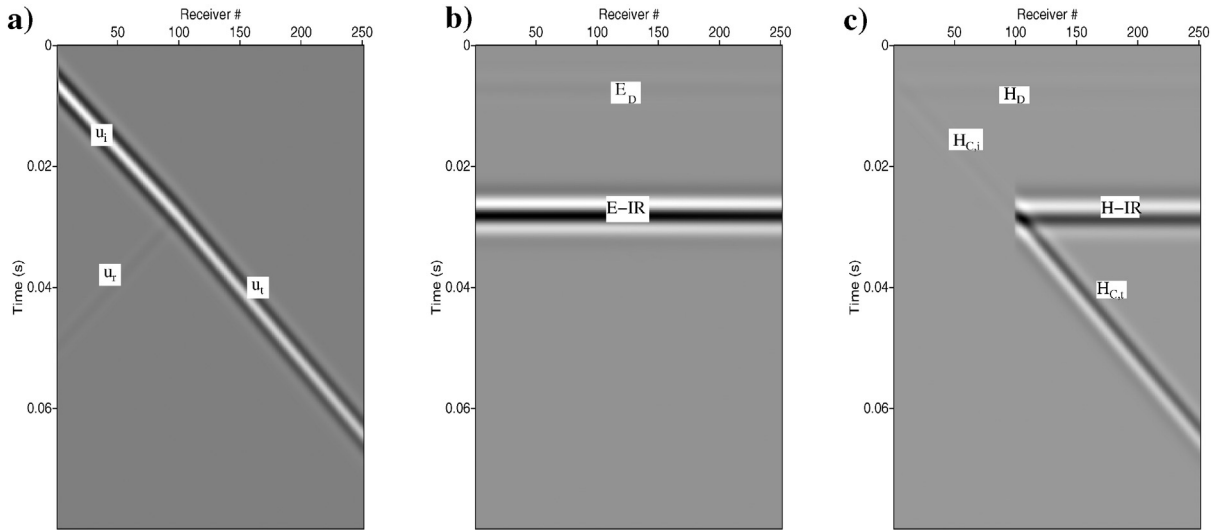| Fluid properties	
ρ_w [kg/m³]	1000
ρ_{LNAPL} [kg/m³]	1620
ρ_{DNAPL} [kg/m³]	750
ρ_{air} [kg/m³]	1.18
η_w [Pa·s]	$1 \cdot 10^{-3}$
η_{DNAPL} [Pa·s]	$8 \cdot 10^{-4}$
η_{LNAPL} [Pa·s]	$4 \cdot 10^{-4}$
η_{air} [Pa·s]	$2 \cdot 10^{-5}$
c_w [ppt]	1

Fig. 3. Results obtained with the FE-algorithm using as seismic source an infinite shear plane acting along x, as described in Section 5; recall that solid and fluid displacement and electric field have only x component and magnetic field has only y component. (a) Horizontal solid displacement u_j, $j =$ i (incident), r (reflected), t (transmitted); (b) horizontal electric field E, subscript D stands for direct, i.e. the field originated as a conversion at the source; subscript IR is associated to the interface response generated at 24.5 m depth, (c) horizontal magnetic field H; the subscript D stands for direct, C for coseismic, subscript IR is associated to the H-IR generated at 24.5 m depth.

new interpretation, we now solve Maxwell's equations, neglecting displacement currents, for a one dimensional model. As EM source, we consider an infinite current sheet flowing along the x axis located at a depth $z_f = 2000$ m and an in-depth recording array composed of 401 electromagnetic receivers spaced 10 m, so that there were receivers on either side of the source. The time signature considered for the EM source is a Ricker wavelet of frequency $f_{peak} = 120$ Hz. The reader might notice that the range of depths considered for this particular synthetic experiment is different from the range proposed on the Results section. This choice relies on the fact that if greater depth ranges are considered, it is easier to visualize the diffusive behavior of the EM fields. However, as it will be discussed later on the paper, the results obtained in this section can be easily extrapolated to length scales of tenths of meters. As we mentioned, Pride's equations and their one dimensional version for the SHTE case are given in Appendix B; there it is also indicated that the finite element formulation is used to find the numerical approximation to their solution. In this section, according to the considered situation, we use only Eqs. (B.7), (B.8) and (B.12), replacing the right hand side of the first one by $J_e(\omega,z) = J(\omega)\delta(z - z_f)$, the mathematical description for the current sheet described above. Here, $J(\omega)$ is the Fourier transform of its time signature.

As a first case we consider a homogeneous medium with conductivity $\sigma = 10^{-7}$ S/m. As we show in Fig. 1a, the resulting electric field $E \equiv E_x$ is continuous and almost constant. The resulting magnetic field $H \equiv H_y$ presents inverse polarities on either side of the source, but its amplitude remains also almost constant. As a second case, we consider $\sigma = 10^{-2}$ S/m. As it can be seen in Fig. 1b, both fields strongly decrease as they diffuse away from the source; it is possible to distinguish a slope given by $v = \sqrt{2\omega/\mu\sigma}$. As a third case we consider a 2000 m thick layer with conductivity $\sigma_1 = 10^{-2}$ S/m, set on top of a half-space with conductivity $\sigma_2 = 10^{-3}$ S/m. As one can see in Fig. 1c, E is continuous at the interface and its amplitude strongly decreases in the upper layer. Inversely, H is discontinuous at the interface and its greatest amplitudes correspond to the upper layer. We next consider $\sigma_1 = 10^{-2}$ S/m and $\sigma_2 = 10^{-5}$ S/m. As one can see in Fig. 1d, the pattern is similar to the one described above, except for the fact that E is constant and H is not noticeable in the lower layer. Finally, we reverse both conductivities; the fields present correspondingly the same behavior.

The IRs generated at the different interfaces considered below follow the same pattern as the ones described in this section. Therefore, we make an alternative interpretation to what was stated by Haines and Pride (2006), and consider that a shear wave will induce a current
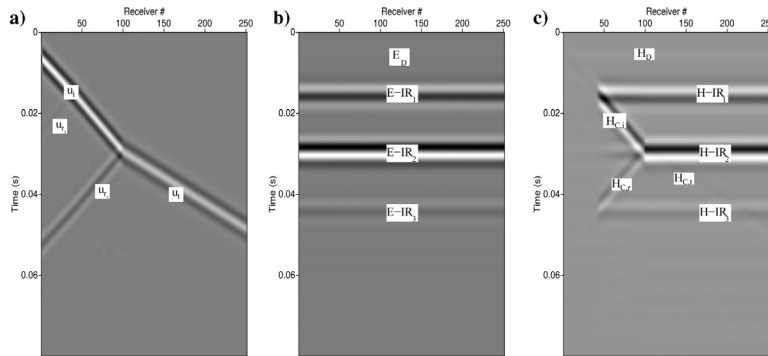

Fig. 4. Results obtained with the geometry described in Section 5, recall that solid and fluid displacement and electric field have only x component and magnetic field has only y component. (a) Horizontal solid displacement u_j, $j =$ i (incident), r (reflected), t (transmitted); (b) horizontal electric field E, subscript D stands for direct, i.e. the field originated as a conversion at the source; subscript IR is associated to the interface response generated at 24.5 m depth; (c) horizontal magnetic field H; the subscript D stands for direct, C for coseismic, subscript IR is associated to the H-IR generated at 24.5 m depth.

sheet along the interface, which in turn is responsible for the observed IRs. Further research, considering Fresnel zones for the S-waves, in a similar fashion to what Garambois and Dietrich (2002) did for P-waves, is necessary to completely understand the conversion process taking place in the situation analyzed in this work.

5. Model description

Models proposed to simulate the presence of DNAPLs and LNAPLs are summarized in Fig. 2. In the DNAPL-case, we consider a simple tabular model consisting of 3 layers, with the same mineral frame, set on top of a less porous half-space. Layer 1 (L_1), 10 m thick and partially saturated, represents the vadose zone. Layer 2 (L_2) models a fresh water aquifer, so it is fully saturated with water. Layer 3 (L_3), whose thickness we call h, is fully saturated with a water/DNAPL mixture. All their properties are detailed in Table 1. In order to simulate a seal rock, the

half-space porosity is chosen so that κ_0 is, at least, 3 orders of magnitude smaller than for the top layers.

In the LNAPL-case, we consider 3 layers characterized by the same mineral frame. Layer 1 (L_1), representing the vadose zone, is partially saturated. Layer 2 (L_2), whose thickness is called h, is fully saturated with a water/LNAPL mixture. Layer 3 (L_3) corresponds to a fully saturated half-space. All their properties are detailed in Table 1. In all cases, the validity of the thin-double-layer approximation was verified.

As seismic source, we consider an infinite shear source oriented along x set at a depth $z_s = 0.01$ m; being its signature a Ricker wavelet, or "Mexican hat" wavelet, of peak frequency $f_{peak} = 150$ Hz. Seismoelectric signals are recorded by a vertical array which consists of 250 seismic and electromagnetic transverse receivers, evenly spaced at intervals of 0.25 m so that there are receivers on either side of the contaminated layer. It is worth noting that due to the geometry considered, only solid displacements $u_x^s(z)$ and fluid displacements $u_x^f(z)$ are
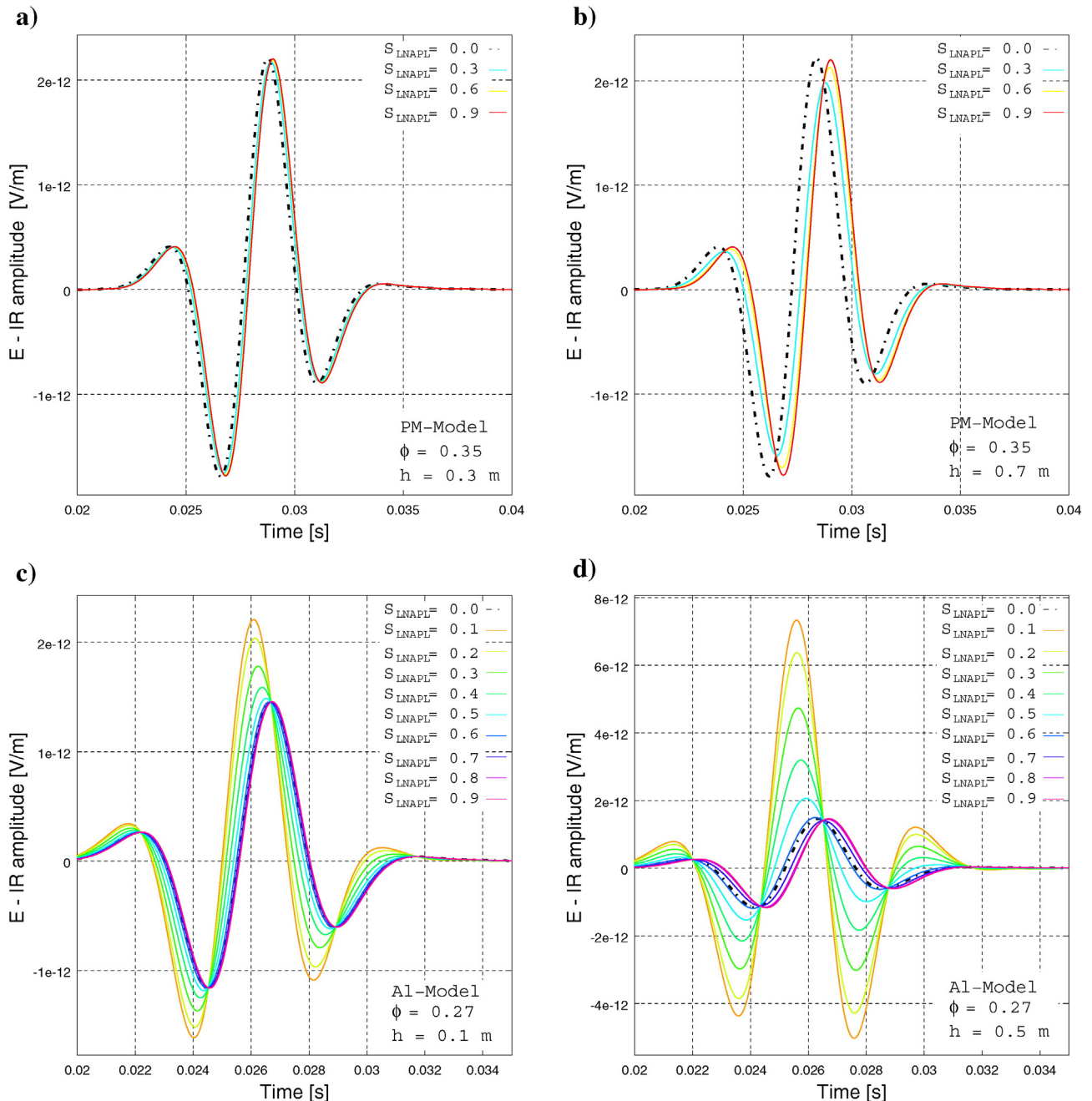

Fig. 5. Electric field interface response E-IR dependence on LNAPL saturation S_{LNAPL}. Panels (a)–(b) correspond to PM-Model and panels (c)–(d) correspond to Al-Model.
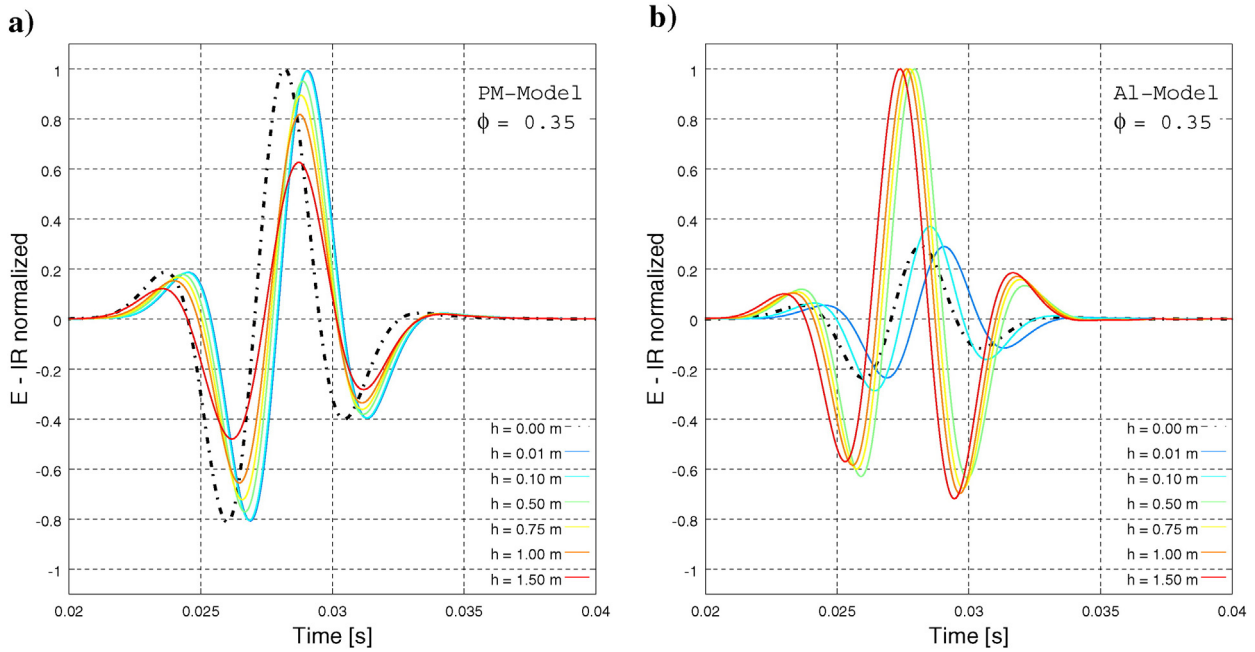
a)

b)

Fig. 6. Electric field interface response E-IR dependence on the thickness of the contaminated layer h for: a) PM-Model; b) Al-Model. Notice that in (b) it is possible to clearly identify different responses even for thicknesses as small as $h = 0.01$ m.

possible. Therefore, we have $E \equiv E_x(z)$ and $H \equiv H_y(z)$. As mentioned in Zyserman et al. (2015), a pure SH seismic source could achieve a better resolution than the one obtained through the usual P-driven experiments because of shorter wavelengths. For S-wave sources for field applications, the reader can see Krawczyk et al. (2012); Crane et al. (2013) and references therein.

6. Results

Let us begin our analysis considering the LNAPL case. In Fig. 3a, where the horizontal solid displacement is shown, one can notice the downgoing direct S-wave u_i. When this direct wave hits the interface located at 24.50 m depth (receiver #98) at about 0.025 s, a small part of the total incident energy reflects back to the surface as an upgoing S-wave u_r. The downgoing transmitted S-wave u_t travels at the same velocity as u_i because the contrast between the layers is due to fluid content, and, as it is known, S-wave velocity is not sensitive to this parameter. In Fig. 3b, displaying the electric field, one can distinguish two events. One of them, with zero moveout, —labeled as E_D in this figure – is "simultaneous" with the source triggering. This flat arrival may be related to the direct field predicted by Pride and Haartsen (1996) and measured by Haines (2004). The second event, which we associate with an Interface Response (E-IR), arises at about 0.025 s, that is, at about the time needed for the S-wave to reach the interface. As stated in Haines and Pride (2006), there is no distinguishable coseismic electric field for S-waves, but the coseismic magnetic field is present, as one can observe in Fig. 3c. The amplitude of the magnetic IR (H-IR) is relatively small in the upper layers and shows inverted polarities on each side of the interface; notice that this behavior is compatible with the analysis done in Section 4, where the discontinuous H takes smaller values in relatively low conductivity regions. Then, the E-IR may be easier to be detected than the H-IR for a receiver located at the earth's surface.

The behavior observed in the DNAPL case, which is shown in Fig. 4, is similar to the one described above; the main difference lies in the fact that two reflected waves u_{r_1} and u_{r_2} are observed. Besides, the downgoing transmitted S-wave u_t travels at a higher velocity than u_i

due to the contrast in the mineral frame properties. In Fig. 4b, displaying the electric field, besides noticing that it is continuous across the interfaces and its amplitude remains almost constant, one can distinguish four events namely: E_D related to the direct field; E-IR$_1$ at 10 m depth (receiver #40) associated to the bottom of the vadose zone; E-IR$_2$ located at 24.50 m depth (receiver #98) at about 0.025 s, that we associate with the presence of the contaminated layer; and E-IR$_3$ generated at the vadose zone when the reflected wave u_{r_2} reaches this layer. In Fig. 4c it is possible to notice that the amplitude of the H-IR$_1$
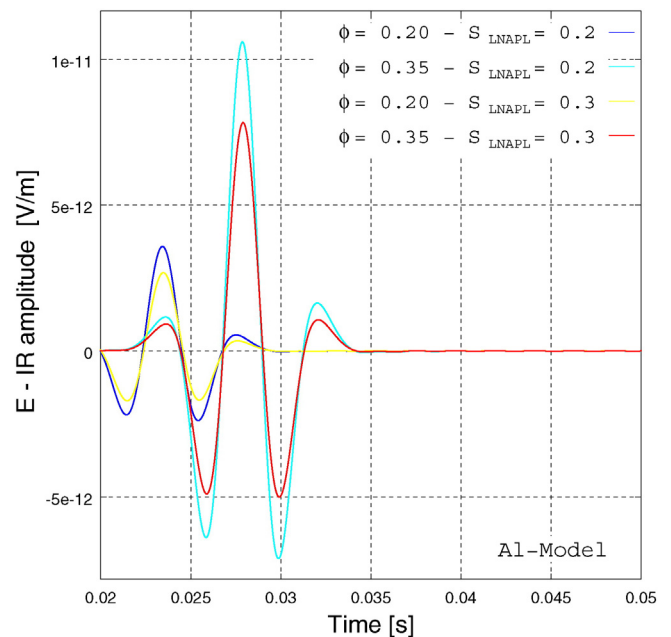

Fig. 7. Electric field interface response E-IR dependence on the porosity. Although the results showed correspond to Al-Model, they are valid for all saturation functions considered in this work.

in L_1 is lower than the amplitude of the H-IR$_2$ in L_2, and both responses are smaller than the respective ones in the fully water saturated semispaces, situation again compatible with the assumption that the IRs are originated by current sheets. As in the LNAPL case, from now on, electric and magnetic IRs of interest E-IR$_2$ and H-IR$_2$ will be denoted as E-IR and H-IR, respectively.

6.1. LNAPL case

Our next step is to analyze the sensitivities of E-IR and H-IR to changes in model parameters. We observe that both IRs follow the same variation pattern, but there is a difference in about 2% in the relative changes for all parameters between them. The origin of this difference could be partially due to a numerical artifact because different approximating functions are used to solve each field in the finite element

algorithm. Therefore we take the E-IR and the H-IR as equally sensitive to changes in the contaminated layer properties.

Based on the analysis described above, our study will be focused on the E-IR recorded by a receiver located at the Earth's surface (receiver #1).

6.1.1. Influence of the LNAPL saturation

In this section we study the influence of the LNAPL saturation (S_{LNAPL}) on the E-IR. The behavior observed depends on $C(S_{\mathrm{w}})$; for $C^{PM}(S_{\mathrm{w}})$, if $h < 0.5$ m, it is not possible to clearly separate the different responses, as it is shown in Fig. 5a. As can be seen in Fig. 5b, for $h > 0.5$ m, the IR amplitude increases when LNAPL saturation is increased. Besides, a displacement to greater times is observed with increasing S_{LNAPL}. However, these differences only allow us to discern between low and high LNAPL contents. On the contrary, for $C^{AI}(S_{\mathrm{w}})$, it is
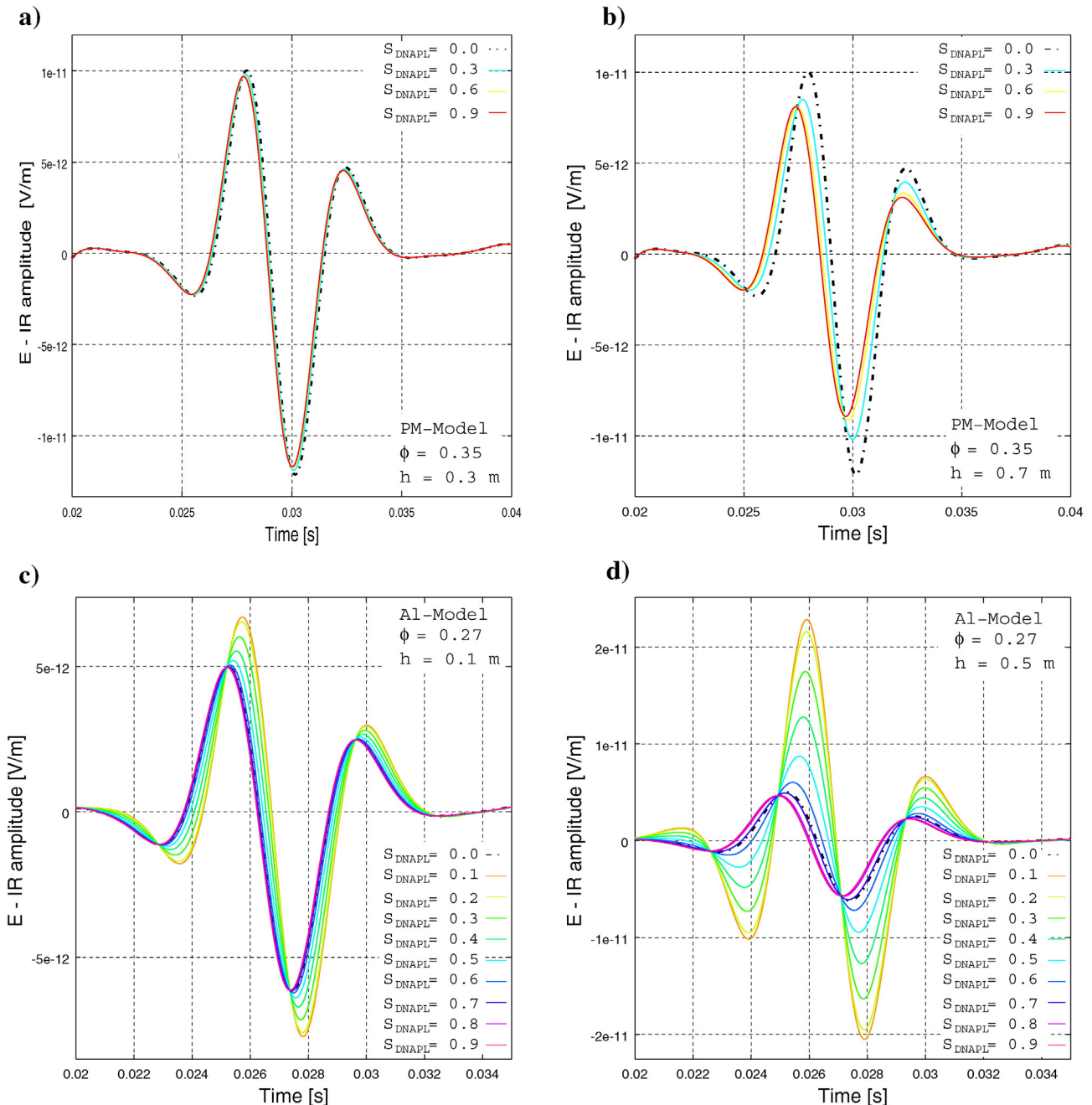

Fig. 8. Electric field interface response E-IR dependence on DNAPL saturation S_{DNAPL} for: (a)–(b) PM-Model; (c)–(d) Al-Model.

possible to distinguish changes in the IR even for $h = 0.1$ m, as we show in Fig. 5c. It is observed that the IR amplitude decreases and responses move to greater times when LNAPL saturation is increased. Besides, for 0.1 m $< h <$ 0.3 m, the responses associated to LNAPL saturation equal to 0, 0.6, 0.7, 0.8 and 0.9 are coincident. For $h >$ 0.3 m, it is possible to clearly identify all responses, as it is shown in Fig. 5d. It is worth noting that the highest amplitudes recorded correspond to $0.1 < S_{LNAPL} < 0.4$ due to the non-monotonic behavior of the Allègre saturation function. For $C^C(S_w)$, results are analogous to those observed for $C^{PM}(S_w)$; except from the fact that it is not possible to clearly separate the different responses for $h <$ 0.75 m and time shifts are not observed.

6.1.2. Influence of the contaminated layer thickness

We study the influence of the contaminated layer thickness (h) on the IR. In order to proceed, we fix $S_{LNAPL} = 0.3$ and consider 0.01 m $< h <$ 3 m. The results are normalized with respect to the maximum value of the maximum amplitude of all recorded IRs. Our results are shown in Fig. 6. When considering $C^{PM}(S_w)$, for 0.01 m $< h <$ 0.1 m, responses are coincident. For 0.15 m $< h <$ 2.5 m, the IR amplitude decreases and moves to shorter times when h increases. Because of this behavior, we call $h = 0.15$ m a threshold thickness (h_c). However, as it will be discussed later, IR amplitudes and h_c values depend on porosity. For $h >$ 2.5 m, two different IRs, associated with the top and bottom of the contaminated layer, can be identified. Moreover, when $C^C(S_w)$ is considered, the behavior observed is similar to the one described, except from the fact that the relative differences between IRs are smaller. On the other hand, when $C^{Al}(S_w)$ is considered, it is possible to distinguish the responses even for $h = 0.01$ m; therefore, in this case, $h_c = 0.01$ m. For $h_c < h <$ 0.5 m, the IR amplitude strongly increases when h is increased and IRs move to shorter times. For 0.5 m $< h <$ 2.5 m, the IR amplitude weakly increases as h takes higher values. It is important to mention that, for all saturation functions considered in this paper, all responses differ from the one due to the absence of contamination ($h = 0$ m).

6.1.3. Influence of the porosity

We analyze the influence of porosity on the IR; the following analysis is valid for all saturation functions considered in this work. In order

to proceed, we consider different scenarios fixing all parameters except for the porosity; values considered can be found in Table 1. In order to handle realistic situations, we modify the porosity of all the layers instead of just changing the porosity of the contaminated layer. Fig. 7 summarizes the main results. As expected, porosity plays an important role in the amplitude of the IRs. We observe that the IR amplitude increases when porosity is increased. In addition, IRs move to shorter times when porosity is decreased, due to changes in the shear wave velocity V_s. Besides, the relative contrast between responses due to different LNAPL content or thicknesses, increases as porosity takes higher values. Notice that this analysis is valid also for the DNAPL case.

6.2. DNAPL case

As in the LNAPL case, our analysis will be focused on the E-IR recorded by a receiver located at the Earth's surface.

6.2.1. Influence of the DNAPL saturation

In this section we study the influence of the DNAPL saturation (S_{DNAPL}) on the E-IR. As in the LNAPL case, the behavior observed depends on $C(S_w)$; for $C^{PM}(S_w)$, if $h <$ 0.5 m, it is not possible to clearly separate the different responses, as it is shown in Fig. 8a. As can be seen in Fig. 8b, for $h >$ 0.5 m, the IR amplitude decreases and a displacement to shorter times is observed when S_{DNAPL} is increased. However, as in the LNAPL case, these differences only allow us to discern between low and high DNAPL contents. For $C^C(S_w)$, results are analogous to those described for $C^{PM}(S_w)$; except from the fact that it is not possible to clearly separate the responses for $h <$ 0.75 m and time shifts are not observed. On the contrary, for $C^{Al}(S_w)$, it is possible to distinguish changes in the IR even for $h = 0.1$ m. As it is shown in Fig. 8c, the observed behavior results similar to the one described above, except from the fact that, for 0.1 m $< h <$ 0.3 m, the responses associated to DNAPL saturation equal to 0, 0.6, 0.7, 0.8 and 0.9 are coincident. For $h >$ 0.3 m, it is possible to clearly identify the response associated to $S_{DNAPL} = 0.6$. However, it is not possible to discern between $S_{DNAPL} = 0$ and $S_{DNAPL} = 0.7$. The same happens for $S_{DNAPL} = 0.8$ and $S_{DNAPL} = 0.9$. It is worth noting that, as in the LNAPL case, the highest amplitudes recorded correspond to $0.1 < S_{DNAPL} < 0.4$ due to the non-monotonic behavior of the Allègre saturation function.
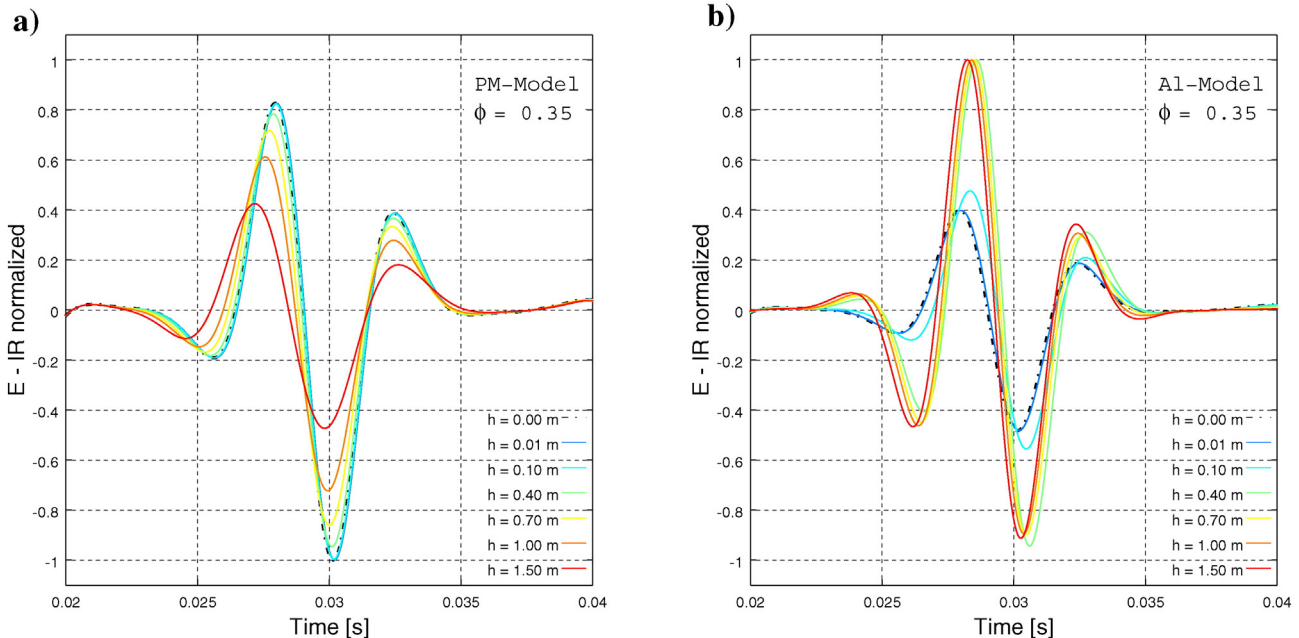

Fig. 9. Electric field interface response E-IR dependence on the thickness of the contaminated layer h for: a) PM-Model; b) Al-Model. Notice that for both models the responses related to the absence of contamination ($h = 0$ m) and $h = 0.1$ m are coincident, as expected.

6.2.2. Influence of the contaminated layer thickness

We study the influence of the contaminated layer thickness h on the IR. In order to do that, we fix $S_{\mathrm{DNAPL}} = 0.3$ and consider $0.01\,\mathrm{m} < h < 3\,\mathrm{m}$. As in the LNAPL case, results are normalized with respect to the maximum value of the maximum amplitude of all recorded IRs, which, in this case, corresponds to absence of contamination. Our results are shown in Fig. 9. For $0.01\,\mathrm{m} < h < 0.1\,\mathrm{m}$, responses are coincident to the one associated with $h = 0\,\mathrm{m}$, i.e., full water saturation. For $0.15\,\mathrm{m} < h < 0.5\,\mathrm{m}$, when h increases the IR amplitude decreases so weakly, that it is not possible to clearly discern the responses. For $0.5\,\mathrm{m} < h < 2.5\,\mathrm{m}$, the IR amplitude strongly decreases when increasing h. Because of this behavior, we consider $h_c = 0.5\,\mathrm{m}$. Moreover, for $h > 0.5\,\mathrm{m}$, the IR moves to shorter times when h increases; we consider that this happens because of the interferences between the IRs generated at the top and bottom of layer L_3. We observe that h_c decreases with higher porosities; for example, if $\phi = 0.35$, then $h_c = 0.40\,\mathrm{m}$, as can be seen in Fig. 9. Also, the time shifts mentioned above become more noticeable at higher porosities. These results are valid for $C^{PM}(S_{\mathrm{w}})$. On the contrary, when $C^C(S_{\mathrm{w}})$ is considered, it is not possible to distinguish the responses even for the highest h value. We consider that this is due to the fact that, for $C^C(S_{\mathrm{w}})$, the IR is mainly governed by the contrast in mechanical properties; so the IR generated at the bottom of the contaminated layer is much greater than the IR generated at the top and, as a consequence, the interference described above is negligible. On the other hand, when $C^{Al}(S_{\mathrm{w}})$ is used, IRs associated with $h < 0.10\,\mathrm{m}$ and the absence of contamination are coincident; as a consequence, we take $h_c = 0.10\,\mathrm{m}$. For $h_c < h < 0.5\,\mathrm{m}$, the IR amplitude increases when h is increased and IRs move to higher times. For $0.5\,\mathrm{m} < h < 2.5\,\mathrm{m}$, the IR amplitude weakly increases and the maximum amplitude moves to shorter times when h increases. In order to explain this pattern, we consider $h = 15\,\mathrm{m}$, so that the IRs of the top and bottom of the contaminated layer can be clearly distinguished. We observe that the amplitude of the IR generated at the top of the layer is considerably smaller than bottom one and their polarities are inverted. From these results we interpret that, if $h_c < h < 0.5\,\mathrm{m}$ the IRs interfere destructively, however, this interference decreases as h increases. As a consequence, if $h > 0.5\,\mathrm{m}$, the resulting IR is mostly governed by the contrast between the contaminated layer and the half-space parameters.

6.2.3. Viscosity dependence

We study the sensitivity of the IR to changes in viscosity. In this light, we propose different scenarios fixing all parameters except the DNAPL viscosity; for which we consider three different values: $\eta_{\mathrm{DNAPL}} = 0.0008, 0.008$ and $0.08\,\mathrm{Pa.s}$. Although differences in effective viscosity are observed, the IRs obtained are coincident, so we conclude that the Interface Response is not sensitive to changes in the viscosity of the contaminant.

7. Conclusions

In this paper we numerically analyzed whether shear wave driven seismoelectrics can provide useful information to determine the presence of NAPLs, either dense or light, in a fresh water aquifer. We used the extended Pride's formulation for the electrokinetic coupling for the case of partially saturated media recently presented in Warden et al. (2013) to take into account the presence of NAPLs in our model. Moreover, we studied the electric and magnetic Interface Responses using Perrier–Morat and Allègre formulas in the partial NAPL saturation version of the electrokinetic coupling. We resorted to effective medium approaches for the model parameters, and solved Pride's equations by means of a finite element method algorithm. Sensitivity analysis of the E-IR for NAPL saturation, thickness of the contaminated layer, porosity and viscosity were performed.

Regarding the variation of the IR amplitude with depth, in the one dimensional geometry considered, it was observed that the E-IR is continuous across the interfaces and its amplitude remains almost constant. However, the H-IR is discontinuous, being its amplitude in the considered scenarios up to three orders of magnitude smaller above the interface than below it, and presents a polarity inversion. These behaviors are compatible with considering a current sheet located at the interface as source of the IRs. As a direct consequence of the observed patterns, in data acquisition, it would be reasonable to locate magnetic receivers under the target interface.

We also analyzed the sensitivities of E-IR and H-IR to changes in model parameters, concluding that E-IR and H-IR could be considered as equally sensitive to changes in the contaminated layer properties.

Concerning the influence of the NAPL saturation on the E-IR, the behavior observed depends on the water saturation function $C(S_{\mathrm{w}})$ considered; for $C^{PM}(S_{\mathrm{w}})$, differences only allow us to discern between low and high NAPL contents for $h > 0.5\,\mathrm{m}$. For $C^C(S_{\mathrm{w}})$, it is not possible to clearly separate the different responses for $h < 0.75\,\mathrm{m}$. On the contrary, for $C^{Al}(S_{\mathrm{w}})$, it is possible to distinguish changes in the IR even for $h = 0.1\,\mathrm{m}$. However, if $h < 0.3\,\mathrm{m}$, there is an important degree of ambiguity for $S_{\mathrm{LNAPL}} > 0.6$ due to the non-monotonic behavior of the Allègre saturation function. In the LNAPL case, for $h > 0.3\,\mathrm{m}$, this ambiguity completely disappears, however it remains present in the DNAPL case. These results show that seismoelectrics is sensitive to the presence of NAPLs and changes in their content. However, the method's resolution will depend on which saturation function is more adequate to describe the electrokinetic phenomenon.

When studying the influence of the contaminated layer thickness on the IR, we observed that seismoelectrics is sensitive to the presence of NAPL as from a threshold thickness h_c. This value strongly depends on the type of contaminant and the saturation function considered. In the LNAPL case, for $C^{PM}(S_{\mathrm{w}})$ and $C^C(S_{\mathrm{w}})$, $h_c = 0.15\,\mathrm{m}$; for $C^{Al}(S_{\mathrm{w}})$, $h_c = 0.01\,\mathrm{m}$. In the DNAPL case, for $C^{PM}(S_{\mathrm{w}})$, $h_c = 0.5\,\mathrm{m}$; and for $C^{Al}(S_{\mathrm{w}})$, $h_c = 0.10\,\mathrm{m}$. Unfortunately, for $C^C(S_{\mathrm{w}})$ it is not possible to identify different responses even for the highest h value. Also, we observed that h_c depends on the porosity; resulting that h_c decreases when porosity is increased.

As expected, porosity plays an important role in the amplitude of the IRs. We observed that the amplitude of the Interface Response increases when porosity is increased. In addition, the relative contrast between responses, due to different NAPL content, increases as porosity takes higher values. On the contrary, we did not observe significative changes in IRs when varying the viscosity of the contaminant.

We expect that the novel results presented in this work will be followed by other necessary developments, such as a higher-dimensional analysis, which will allow us to model more realistic geological environments and determine if the absolute amplitudes of the IR are large enough to be detected. On the other hand, these results show the need of developing new studies about the influence of NAPL on the electrokinetic coupling; considering, for example, the generation of an electrical double layer at the interface NAPL–water. We also expect that the results shown in this work will encourage field tests, which should in the end determine if seismoelectric can provide useful information to detect the presence of NAPLs and, eventually, will lead to a new monitoring tool which complements the existing ones.

Appendix A. $L(\omega)$ and σ models

According to Pride (1994),

$$L(\omega) = L_0 \left[1 - i \frac{\omega}{\omega_j} \frac{b}{4} \left(1 - 2\frac{d}{\Lambda} \right)^2 \left(1 - i^{3/2} d \sqrt{\frac{\omega \rho_w}{\eta_w}} \right)^2 \right]^{-1/2}, \qquad (A.1)$$

where the low frequency electrokinetic coupling coefficient L_0 is given by

$$L_0 = -\frac{\phi}{\alpha_\infty} \frac{\varepsilon_w \zeta}{\eta_w} \left(1 - 2\frac{d}{\Lambda} \right). \qquad (A.2)$$

In Eqs. (A.1) and (A.2), Λ [m] is a pore geometrical parameter, defined in Johnson et al. (1987), b is a dimensionless parameter defined in terms of the latter, the porosity ϕ, the absolute permeability κ_0 and the tortuosity α_∞ as $b = (\phi/\alpha_\infty \kappa_0)\Lambda^2$ and consisting only of the pore-space geometry terms. This parameter b was originally denoted m in Pride (1994). When κ_0, ϕ, α_∞ and Λ are independently measured, $4 < b < 8$ for different porous media ranging from grain packing to capillary networks consisting of tubes of variable radii (Johnson et al., 1987). The parameter ω_j is the permeability-dependent transition angular frequency between the low-frequency viscous flow and high-frequency inertial flow, while d [m] is the Debye length, a measure of the thickness of the diffuse double layer, given by the expression

$$d = \left(\sum_{l=1}^{2} \frac{(ez_l)^2 N_l}{\eta_w kT} \right)^{-1/2}, \qquad (A.3)$$

where $k = 1.38 \cdot 10^{-23}$ J/K is Boltzmann's constant, T is temperature in Kelvin (which we assume 298 K), $e = 1.6 \cdot 10^{-19}$ C is the electric charge of the ions, z_l is the valence and N_l is the bulk ionic concentration. For salt water, $z_1 = 1$ (cation), $z_2 = -1$ (anion) and $N_1 = N_2 = N$ (Carcione et al., 2003). We use $N = 10^3 c_w N_a$, where c_w is water salinity in mol/l and N_a is Avogadro's number ($6.022 \cdot 10^{23}$ mol^{-1}). The factor 10^3 is introduced in order to express N in ions/m^3.

In Eq. (14) we estimate σ, where C_{em} and C_{os} are computed as (Pride, 1994)

$$C_{em} = 2dN \sum_{l=1}^{2} (ez_l)^2 b_l \left[\exp\left(-\frac{ez_l \zeta}{2kT} \right) - 1 \right], \qquad (A.4)$$

$$C_{os} = \frac{(\epsilon_w \zeta)^2 P}{2d\eta_w} \left(1 - \frac{2i^{3/2} d}{P\delta} \right)^{-1}, \qquad (A.5)$$

where $\delta = (\eta_w/\omega \rho_w)^{1/2}$ is the viscous skin depth and ζ is the zeta potential.

Finally, the parameter P in Eq. (A.5) is computed as

$$P = \frac{8kTd^2N}{\epsilon_w \zeta^2} \sum_{l=1}^{2} \left[\exp\left(-\frac{ez_l \zeta}{2kT} \right) - 1 \right]. \qquad (A.6)$$

Appendix B. One dimensional SHTE equations

Consider Pride's equations in the equivalent form given in Zyserman et al. (2012)

$$(\sigma + i\epsilon\omega)\boldsymbol{E} - \nabla \times \boldsymbol{H} + L(\omega)\eta_f k^{-1}(\omega)\left[i\omega \boldsymbol{u^f} - L(\omega)\boldsymbol{E} \right] = -\boldsymbol{J_e^{ext}}, \qquad (B.1)$$

$$\nabla \times \boldsymbol{E} + i\omega\mu\boldsymbol{H} = -\boldsymbol{J_m^{ext}}, \qquad (B.2)$$

$$-\omega^2 \rho_b \boldsymbol{u^s} - \omega^2 \rho_f \boldsymbol{u^f} - \nabla \cdot \tau(\boldsymbol{u}) = \boldsymbol{F^{(s)}}, \qquad (B.3)$$

$$-\omega^2 \rho_f \boldsymbol{u^s} + \eta_f k^{-1}(\omega)\left[i\omega \boldsymbol{u^f} - L(\omega)\boldsymbol{E} \right] + \nabla p_f = \boldsymbol{F^{(f)}}, \qquad (B.4)$$

$$\tau_{lm}(\boldsymbol{u}) = 2G_b \, \varepsilon_{lm}(\boldsymbol{u^s}) + \delta_{lm}\left(\lambda_c \nabla \cdot \boldsymbol{u^s} + \alpha K_{av} \nabla \cdot \boldsymbol{u^f} \right), \qquad (B.5)$$

$$p_f(\boldsymbol{u}) = -\alpha K_{av} \nabla \cdot \boldsymbol{u^s} - K_{av} \nabla \cdot \boldsymbol{u^f}. \qquad (B.6)$$

Here τ and ε are the stress and strain tensors, $\rho_b = \phi\rho_f + (1-\phi)\rho_s$ the bulk density, G_b is the shear modulus, K_{av} is the fluid-storage coefficient and αK_{av} is the Biot coupling coefficient, with $\alpha = 1 - K_{fr}/K_s$. In the seismic frequency regime, for most fluid saturated rocks, displacement currents can be safely neglected against conduction currents in the factor multiplying the electric field $\boldsymbol{E}$ in the first term of Eq. (B.1). Besides, as it has been demonstrated (Hu and Liu, 2002), if $\eta L^2(\omega)/(\sigma k(\omega)) \ll 1$, the electroosmotic feedback can be neglected in Biot's equations, and the latter decouples from Maxwell's equations. As we are dealing with just seismic shear sources, we set the electromagnetic sources, and the seismic source acting upon the fluid to zero, $\boldsymbol{J_m^{ext}} = \boldsymbol{J_e^{ext}} = \boldsymbol{F^{(f)}} = 0$. Moreover, as $\boldsymbol{F^{(s)}}$ is considered to be a shearing force parallel to the x axis acting on a horizontal infinite plane upon a horizontally layered Earth, only solid displacements $\boldsymbol{u^s} \equiv u_x^s(z,\omega)$ and average relative fluid displacements $u^f \equiv u_x^f(z,\omega)$ are possible. Therefore, we have $E \equiv E_x(z,\omega)$ and $H \equiv H_y(z,\omega)$. Under these considerations, Eqs. (B.1)–(B.6) can be rewritten as

$$\sigma E - \partial_z H = i\omega\eta_f k^{-1}(\omega)L(\omega)u^f, \qquad (B.7)$$

$$\partial_z E + i\omega\mu H = 0, \qquad (B.8)$$

$$-\omega^2 \rho_b u^s - \omega^2 \rho_f u^f - \partial_z(G_b u^s) = F^{(s)}, \qquad (B.9)$$

$$-\omega^2 \rho_f u^s + i\omega\eta_f k^{-1}(\omega) \, u^f = 0, \qquad (B.10)$$

where we use ∂_z to denote the derivative with respect to z. Notice that, although we do not consider it, in the seismic frequency range it is usual to take the low frequency limit for the electrokinetic coupling coefficient and the dynamic permeability; in this case we would have $i\omega(\eta_f/k_0)L_0 u^f$ as the r.h.s. of Eq. (B.7) and $i\omega\eta_f k^{-1}(\omega) \approx (-\omega^2 g_0 + i\omega\eta/k_0)$ in Eq. (B.10); in this last expression g_0 is the mass coupling coefficient. Finally, following Santos et al. (2004), we express $F^{(s)}$ as

$$F^{(s)}(z,\omega) = F(\omega)\partial_z\delta(z-z_f). \qquad (B.11)$$

Here $F(\omega)$ is the Fourier transform of the seismic source time signature, and the Dirac's delta derivative must be understood in the distributional sense; by z_f we denote the depth at which the source is located. The set of Eqs. (B.7)–(B.10) must be completed with appropriate boundary conditions. For Maxwell's equations we use absorbing boundary conditions (ABC's) at the top and bottom boundaries, for Biot's equations we use the free boundary condition for the air-soil interface and again ABC's at the bottom boundary; see Zyserman et al. (2010, 2012); Pride and Haartsen (1996) and references therein for details. In the present case they read, for Maxwell's equations and Biot's equations respectively:

$$(1-i)\sqrt{\frac{\sigma}{2\omega\mu}}E - \nu H = 0, \qquad (B.12)$$

where ν takes the value -1 at the top boundary and the value 1 at the bottom one,

$$\partial_z u^s = 0 \quad \text{top boundary}, \qquad (B.13)$$

$$-\partial_z u^s = i\omega\left(\rho_b - \rho_f^2/g(\omega)\right)\sqrt{\frac{G_b}{\rho_b - \rho_f^2/g(\omega)}}, \quad \text{bottom boundary}, \text{(B.14)}$$

where $g(\omega) = (1/\omega)\text{Im}(\eta/k(\omega))$. As already stated, the system of Eqs. (B.7)–(B.14) is solved by means of a finite elements procedure.

References

Allègre, V., Jouniaux, L., Lehmann, F., Sailhac, P., 2010. Streaming potential dependence on water-content in Fontainebleau sand. Geophys. J. Int. 182, 1248–1266.

Allègre, V., Lehmann, F., Ackerer, P., Jouniaux, L., Sailhac, P., 2012. Modelling the streaming potential dependence on water content during drainage: 1. A 1D modelling of SP using finite element method. Geophys. J. Int. 189, 285–295.

Allègre, V., Jouniaux, L., Sailhac, P., Toussaint, R., 2015. Influence of water pressure dynamics and fluid flow on the streaming-potential response for unsaturated conditions. Geophys. Prospect. 63, 694–712 (May).

Benson, R., Glaccum, R., Noel, M.R., 1982. Geophysical Techniques for Sensing Buried Wastes and Waste Migration. Natl. Water Well Assoc.

Biot, M.A., 1956a. Theory of propagation of elastic waves in a fluid-saturated porous solid: I. Low frequency range. J. Acoust. Soc. Am. 28 (2), 168–178 (March).

Biot, M.A., 1956b. Theory of propagation of elastic waves in a fluid-saturated porous solid: II. High frequency range. J. Acoust. Soc. Am. 28 (2), 178–191 (March).

Blatze, M.L., Wang, Z., 1992. Seismic properties of pore fluids. Geophysics 11 (57), 1396–1408.

Block, G.I., Harris, J.G., 2006. Conductivity dependence of seismoelectric wave phenomena in fluid-saturated sediments. J. Geophys. Res. 111, B01304.

Bordes, C., Jouniaux, L., Dietrich, M., Pozzi, J.-P., Garambois, S., 2006. First laboratory measurements of seismo-magnetic conversions in fluid-filled Fontainebleau sand. Geophys. Res. Lett. 33, L01302 (jan).

Bordes, C., Jouniaux, L., Garambois, S., Dietrich, M., Pozzi, J.-P., Gaffet, S., 2008. Evidence of the theoretically predicted seismo-magnetic conversion. Geophys. J. Int. 174, 489–504.

Brovelli, A., Cassiani, G., Dalla, E., Bergamini, F., Pitea, D., Binley, A.M., 2005. Electrical properties of partially saturated sandstones: novel computational approach with hydrogeophysical applications. Water Resour. Res. 41 (12 pp.).

Butler, K., 1996. Seismoelectrics Effects of Electrokinetic Origin (PhD Thesis) Univ. B.C. Vancouver, Canada.

Carcione, J., Picotti, S., 2006. P-wave seismic attenuation by slow-wave diffusion: effects of inhomogeneous rock properties. Geophysics 71 (3), O1–O8.

Carcione, J., Seriani, G., Gei, D., 2003. Acoustic and electromagnetic properties of soil saturated with salt water and NAPL. J. Appl. Geophys. 52, 177–191.

Chen, B., Mu, Y., 2005. Experimental studies of seismoelectric effects in fluid-saturated porous media. J. Geophys. Eng. 2, 222–230 (sept).

Crane, J., Lorenzo, J., Harris, J., 2013. A new electrical and mechanically detonatable shear wave source for near surface (0–30 m) seismic acquisition. J. Appl. Geophys. 91, 1–8.

Davis, J.O., 1991. Depth zoning and specializing processing methods for electromagnetic geophysical surveys to remote sense hydrocarbon type groundwater contaminants. Proceedings of the Fifth National Outdoor Action Conference on Aquifer Restoration, Ground Water Monitoring and Geophysical Methods, pp. 905–913.

Dullien, F.A.L., 1991. One and two phase flow in porous media and pore structure. Physics Granular Media, pp. 173–214.

Dupuis, J.C., Butler, K.E., 2006. Vertical seismoelectric profiling in a borehole penetrating glaciofluvial sediments. Geophys. Res. Lett. 33.

Dupuis, J.C., Butler, K.E., Kepic, A.W., 2007. Seismoelectric imaging of the vadose zone of a sand aquifer. Geophysics 72, A81–A85 (Nov–Dec).

Dupuis, J.C., Butler, K.E., Kepic, A.W., Harris, B.D., 2009. Anatomy of a seismoelectric conversion: measurements and conceptual modeling in boreholes penetrating a sandy aquifer. J. Geophys. Res. Solid Earth 114 (B13), B10306 (oct).

Environmental Protection Agency, 1994. DNAPL Site Characterization: Quick Reference Fact Sheet. Tech. Rep. 9355.4-16FS; EPA/540/F-94/049; OSWER-9355.4-16FS. Office of Emergency and Remedial Response, Washington, D.C. (September).

Frenkel, J., 1944. On the theory of seismic and electroseismic phenomena in a moist soil. J. Phys. 8 (4), 230–241.

Gao, Y., Hu, H., 2010. Seismoelectromagnetic waves radiated by a double couple source in a saturated porous medium. Geophys. J. Int. 181, 873–896.

Garambois, S., Dietrich, M., 2001. Seismoelectric wave conversions in porous media: field measurements and transfer function analysis. Geophysics 66, 1417–1430.

Garambois, S., Dietrich, M., 2002. Full waveform numerical simulations of seismoelectromagnetic wave conversions in fluid-saturated stratified porous media. J. Geophys. Res. 107 (B7) (ESE). (5–1).

Guan, W., Hu, H., Wang, Z., 2013. Permeability inversion from low-frequency seismoelectric logs in fluid-saturated porous formations. Geophys. Prospect. 61, 120–133.

Gueguen, Y., Palciauskas, V., 1994. Introduction to the Physics of Rocks. Princeton University Press, Princeton.

Guichet, X., Jouniaux, L., Pozzi, J.-P., 2003. Streaming potential of a sand column in partial saturation conditions. J. Geophys. Res. 108 (B3), 2141.

Haartsen, M.W., Pride, S., 1997. Electroseismic waves from point sources in layered media. J. Geophys. Res. 102, 24,745–24,769.

Haines, S., 2004. Seismoelectric Imaging of Shallow Targets (Ph.D. thesis) Stanford University.

Haines, S.H., Pride, S.R., 2006. Seismoelectric numerical modeling on a grid. Geophysics 71 (6), 57–65.

Haines, S.S., Guitton, A., Biondi, B., 2007a. Seismoelectric data processing for surface surveys of shallow targets. Geophysics 72, G1–G8 (March–April).

Haines, S.S., Pride, S.R., Klemperer, S.L., Biondi, B., 2007b. Seismoelectric imaging of shallow targets. Geophysics 72, G9–G20 (March-April).

Hu, H., Gao, Y., 2011. Electromagnetic field generated by a finite fault due to electrokinetic effect. J. Geophys. Res. 116, 1132–1143 (august).

Hu, H., Liu, J., 2002. Simulation of the converted electric field during acoustoelectric logging. 72nd SEG Annual International Meeting Expanded Abstracts, 21 (Salt Lake City, Utah, USA), pp. 348–351.

Hu, H., Guan, W., Harris, J., 2007. Theoretical simulation of electroacoustic borehole logging in a fluid-saturated porous formation. J. Acoust. Soc. Am. 122, 135–145.

Ivanov, A., 1939. Effect of electrization of earth layers by elastic waves passing through them. Dokl. Akad. Nauk SSR (in Russian) 24, 42–45.

Jackson, M.D., 2010. Multiphase electrokinetic coupling: Insights into the impact of fluid and charge distribution at the pore scale from a bundle of capillary tubes model. J. Geophys. Res. 115, B07206.

Jackson, M., Leinov, E., 2012. On the validity of the "thin" and "thick" double-layer assumptions when calculating streaming currents in porous media. Int. J. Geophys., 897807 (12 pp.).

Johnson, D.L., Koplik, J., Dashen, R., 1987. Theory of dynamic permeability in fluid saturated porous media. J. Fluid Mech. 176, 379–402.

Jougnot, D., Linde, N., 2011. Testing a new approach to model streaming potentials using hydrodynamic characteristics of partially saturated media: laboratory study. AGU Fall Meeting Abstracts 1, 1266.

Jougnot, D., Linde, N., 2013. Self-potentials in partially saturated media: the importance of explicit modeling of electrode effects. Vadose Zone J.

Jougnot, D., Linde, N., Revil, A., Doussan, C., 2012. Derivation of soil-specific streaming potential electrical parameters from hydrodynamic characteristics of partially saturated soils. Vadose Zone J.

Jougnot, D., Rubino, J., Carbajal, M.R., Linde, N., Holliger, K., 2013. Seismoelectric effects due to mesoscopic heterogeneities. Geophys. Res. Lett. 40, 2033–2037.

Jougnot, D., Linde, N., Haarder, E., Looms, M., 2015. Monitoring of saline tracer movement with vertically distributed self-potential measurements at the HOBE agricultural site, Voulund, Denmark. J. Hydrol. 521, 314–327.

Jouniaux, L., Bordes, C., 2012. Frequency-dependent Streaming Potentials: A Review. Int. J. Geophysics vol. 2012. Hindawi Publishing Corporation, p. 648781 (11 pp.).

Jouniaux, L., Ishido, T., 2012. Electrokinetics in Earth Sciences: A Tutorial. Int. J. Geophysics vol. 2012. Hindawi Publishing Corporation, p. 286107 (16 pp.).

Krawczyk, C., Polom, U., Trabs, S., Dahm, T., 2012. Sinkholes in the city of Hamburg—new urban shear-wave reflection seismic system enables high-resolution imaging of subrosion structures. J. Appl. Geophys. 78, 133–143.

Lesmes, D.P., Friedman, S.P., 2005. Relationships between the electrical and hydrogeological properties of rocks and soils. In: Rubin, Y., Hubbard, S.S. (Eds.), Hydrogeophysics. Springer, Dordrecht, The Netherlands, pp. 87–128 (Ch. 4).

Linde, N., 2009. A comment on "characterization of multiphase coupling using a bundle of capillary tubes model" by M.D. Jackson [Journal of Geophysical Research, 113, B04201]. J. Geophys. Res. 114 (B06209).

Linde, N., Jougnot, D., Revil, A., Matthai, S.K., Renard, D., Doussan, C., 2007. Streaming current generation in two-phase flow conditions. Geophys. Res. Lett. 34, LO3306 (feb).

Mavko, G., Mukerji, T., Dvorkin, J., 2009. The Rock Physics Handbook: Tools for Seismic Analysis of Porous Media. Cambridge University Press, The Pitt Building, Trumpington Street, Cambridge CB2 IRP, United Kingdom.

Mayer, A.S., Hassamozadesh, S.M., 2005. Soil and Groundwater Contamination: Nonaqueous Phase Liquids—Principles and Observations. American Geophysical Union, Washington, D.C.

Newell, C.J., Acree, S.D., Ross, R.R., 1995. Light Nonaqueous Phase Liquids. Enviromental Protection Agency.

Perrier, F., Morat, P., 2000. Characterization of electrical daily variations induced by capillary flow in the non-saturated zone. Pure Appl. Geophys. 157, 785–810.

Pride, S., 1994. Governing equations for the coupled electromagnetics and acoustics of porous media. Phys. Rev. B Condens. Matter 50, 15678–15695.

Pride, S.R., 2005. Relationships between seismic and hydrological properties. Hydrogeophysics. Springer, Dordrecht, The Netherlands, pp. 253–291 (Ch. 9).

Pride, S., Haartsen, M.W., 1996. Electroseismic wave properties. J. Acoust. Soc. Am. 100, 1301–1315.

Pride, S., Morgan, F.D., 1991. Electrokinetic dissipation induced by seismic waves. Geophysics 56 (7), 914–925.

Ren, H., Chen, X., Huang, Q., 2012. Numerical simulation of coseismic electromagnetic fields associated with seismic waves due to finite faulting in porous media. Geophys. J. Int. 188, 925–944 (march).

Revil, A., Jardani, A., 2010. Seismoelectric response of heavy oil reservoirs: theory and numerical modelling. Geophys. J. Int. 180, 781–797.

Revil, A., Linde, N., 2006. Chemico-electromechanical coupling in microporous media. J. Colloid Interface Sci. 302, 682–694.

Revil, A., Linde, N., Cerepi, A., Jougnot, D., Matthäi, S., Finsterle, S., 2007. Electrokinetic coupling in unsaturated porous media. J. Colloid Interface Sci. 313, 315–327.

Revil, A., Barnier, G., Karaoulis, M., Sava, P., Jardani, A., Kulessa, B., 2013. Seismoelectric coupling in unsaturated porous media: theory, petrophysics, and saturation front localization using an electroacoustic approach. Geophys. J. Int. 196 (2), 867–884.

Rumpf, H., Gupte, A.R., 1971. Einflüsse der porosität und korngrössenverteilung im widerstandsgesetz der porenströmung. Chem. Ing. Tech. 43, 367–375.

Santos, J., Ravazzoli, C., Gauzellino, P., Carcione, J., Cavallini, F., 2004. Simulation of waves in poro-viscoelastic rocks saturated by immiscible fluids. Numerical evidence of a second slow wave. J. Comput. Acoust. 12, 1–21.

Schakel, M., Smeulders, D., Slob, E., Heller, H., 2011. Seismoelectric interface response: experimental results and forward model. Geophysics 76, N29–N36.

Schakel, M., Smeulders, D., Slob, E., Heller, H., 2012. Seismoelectric fluid/porous-medium interface response model and measurements. Transp. Porous Media 93, 271–282.

Schön, J., 1996. Physical Properties of Rocks — Fundamentals and Principles of Petrophysics. vol. 18. Elsevier Science Ltd., Handbook of Geophysical Exploration, Seismic exploration.

Smeulders, D.M.J., Grobbe, N., Heller, H.K.J., Schakel, M., 2013. Seismoelectric conversion for the detection of porous medium interfaces between wetting and nonwetting fluids. Vadose Zone J.

Strahser, M.H.P., 2007. Near Surface Seismoelectrics in Comparative Field Studies (PhD Thesis) Christian-Albrechts-Universität zu Kiel, Germany.

Strahser, M., Jouniaux, L., Sailhac, P., Matthey, P.-D., Zillmer, M., 2011. Dependence of seismoelectric amplitudes on water-content. Geophys. J. Int. 187, 1378–1392.

Teja, A.S., Rice, P., 1981. Generalized corresponding states method for the viscosities of liquid mixtures. Ind. Eng. Chem. Fundam. 20 (1), 77–81.

Thompson, A.H., Gist, G.A., 1993. Geophysical applications of electrokinetic conversion. Lead. Edge 12, 1169–1173.

Thompson, A., Hornbostel, S., Burns, J., Murray, T., Raschke, R., Wride, J., McCammon, P., Sumner, J., Haake, G., Bixby, M., Ross, W., White, B., Zhou, M., Peczak, P., 2005. Field Tests of Electroseismic Hydrocarbon Detection. SEG Technical Program Expanded Abstracts.

Thompson, A., Sumner, J., Hornbostel, S., 2007. Electromagnetic-to-seismic conversion: a new direct hydrocarbon indicator. Lead. Edge 26, 428–435 (April).

Walther, E.G., Pitchford, A.M., Olhoeft, G.R., 1986. Direct detection of hydrocarbons and organic chemicals with ground penetrating radar and complex resistivity. Conference on Petroleum Hydrocarbons and Organic Chemicals in Ground Water — Prevention Detection and Restoration. Natl. Water Well Assoc., pp. 284–305.

Wang, J., Hu, H., Guan, W., Li, H., 2015. Electrokinetic experimental study on saturated rock samples: zeta potential and surface conductance. Geophys. J. Int. 201 (2), 869–877.

Warden, S., Garambois, S., Jouniaux, L., Brito, D., Sailhac, P., Bordes, C., 2013. Seismoelectric wave propagation numerical modeling in partially saturated materials. Geophys. J. Int. 194, 1498–1513.

Yamazaki, K., 2012. Estimation of temporal variations in the magnetic field arising from the motional induction that accompanies seismic waves at a large distance from the epicentre. Geophys. J. Int. 190, 1393–1403.

Zyserman, F., Gauzellino, P., Santos, J., 2010. Finite element modeling of SHTE and PSVTM electroseismics. J. Appl. Geophys. 72, 79–91.

Zyserman, F., Gauzellino, P., Santos, J., 2012. Numerical evidence of gas hydrate detection by means of electroseismics. J. Appl. Geophys. 86, 98–108.

Zyserman, F.I., Jouniaux, L., Warden, S., Garambois, S., 2015. Borehole seismoelectric logging using a shear-wave source: possible application to CO_2 disposal? Int. J. Greenhouse Gas Control 33, 89–102.